

Automatic Ice Surface and Bottom Boundaries Estimation in Radar Imagery Based on Level-Set Approach

Maryam Rahnemoonfar, *Member, IEEE*, Geoffrey Charles Fox, Masoud Yari, and John Paden, *Member, IEEE*

Abstract—Accelerated loss of ice from Greenland and Antarctica has been observed in recent decades. The melting of polar ice sheets and mountain glaciers has considerable influence on sea level rise in a changing climate. Ice thickness is a key factor in making predictions about the future of massive ice reservoirs. The ice thickness can be estimated by calculating the exact location of the ice surface and subglacial topography beneath the ice in radar imagery. Identifying the locations of ice surface and bottom is typically performed manually, which is a very time-consuming procedure. Here, we propose an approach, which automatically detects ice surface and bottom boundaries using distance-regularized level-set evolution. In this approach, the complex topology of ice surface and bottom boundary layers can be detected simultaneously by evolving an initial curve in the radar imagery. Using a distance-regularized term, the regularity of the level-set function is intrinsically maintained, which solves the reinitialization issues arising from conventional level-set approaches. The results are evaluated on a large data set of airborne radar imagery collected during a NASA IceBridge mission over Antarctica and show promising results with respect to manually picked data.

Index Terms—Global warming, ice thickness, image classification, object recognition, radar.

I. INTRODUCTION

IN RECENT years, global warming has caused severe threats to our environment. Accelerated loss of ice from Greenland and Antarctica has been observed in recent decades [1]. The melting of polar ice sheets and mountain glaciers has considerable influence on sea level rise and ocean currents, potentially leading to the flooding of coastal regions and putting millions of people around the world at risk. Therefore, precise calculation of ice thickness is very important for sea level and flood monitoring. Moreover, the shape of the landscape hidden beneath the thick ice sheets is a key factor in predicting ice flow and their future contribution to

sea level rise in response to a changing climate. The subglacial topography beneath the ice sheets has been investigated using geophysical methods since the 1950s. Radar sensors are one of the instruments that can penetrate through ice and give information about the hidden subglacial topography over large areas. The multichannel coherent radar depth sounder was used during the IceBridge mission [2] to provide important information about ice sheet thickness. Ice thickness can be determined by distinguishing layers of different dielectric constants, such as air, ice, and rock in radar echograms. Fig. 1 shows sample echogram images produced by the radar. The images used in this paper are the CReSIS standard output product [3] and are formed using pulse compression, synthetic aperture radar processing, and multilooking. Full details of the processing are provided in [4]. The horizontal axis is along the flight path, and the vertical axis represents the two-way travel time of the radio wave. The dark line on the top of the image is the boundary between air and ice, while the more irregular lower boundary represents the ice bottom, which is the boundary between the ice and the subglacial topography. The subglacial topography hidden beneath the thick ice sheets can take any shape from smooth to mountainous (Fig. 1).

For ice surface and bottom identification, usually manual (human) picking of radargrams is taken. Manual boundary identification is a very time-consuming and tedious task, which can introduce errors. As radar data volumes continue to increase and to improve the reliability of boundary identification, we seek to develop automatic techniques for this process.

There are several challenges in the automatic processing of ice surface and bottom layers. These challenges can be split into three categories. The first is that the ice bottom may suffer from low signal to interference and noise ratios (SINRs). Low SINR is caused by several factors: 1) signal attenuation while traveling through ice; 2) radar clutter energy; and 3) thermal noise and occasional electromagnetic interference. The second is that the subglacial topography is highly variable on a continental scale ranging from flat to mountainous. Finally, artifacts in the data, such as surface multiples (ringing of the radar signal between the large metal aircraft and the ice surface), can lead to false identification of the ice bottom layer.

In this paper, we propose an automatic technique, which can overcome most of the aforementioned challenges. Here, we propose a novel level-set approach to automatically identify the ice surface and bottom layers in a large data set of radar

Manuscript received July 5, 2016; revised January 4, 2017 and March 25, 2017; accepted April 28, 2017. Date of publication June 5, 2017; date of current version August 25, 2017. (*Corresponding author: Maryam Rahnemoonfar.*)

M. Rahnemoonfar is with the Department of Computing Sciences, Texas A&M University at Corpus Christi, Corpus Christi, TX 78412 USA.

G. C. Fox is with the School of Informatics and Computing, Indiana University Bloomington, Bloomington, IN 47405 USA.

M. Yari is with the Department of Engineering, Texas A&M University at Corpus Christi, Corpus Christi, TX 78412 USA.

J. Paden is with the Center for Remote Sensing of Ice Sheets, The University of Kansas, Lawrence, KS 66045 USA.

Color versions of one or more of the figures in this paper are available online at <http://ieeexplore.ieee.org>.

Digital Object Identifier 10.1109/TGRS.2017.2702200

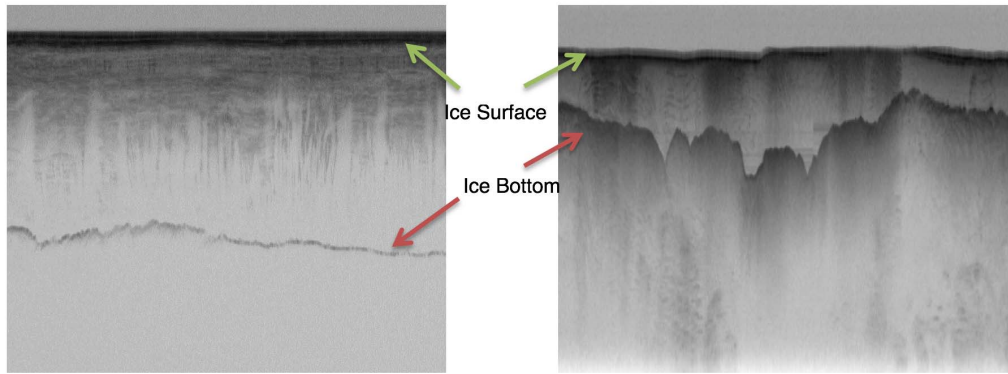


Fig. 1. Ice surface and bottom depicted in radar echograms gathered by the multichannel coherent radar depth.

imagery. In this approach, using an initial curve, the image will be divided into two parts: inside the curve and outside the curve. In the next step, by the help of external and internal forces, each point on the curve starts moving at a variable speed, and the curves will gradually evolve until all boundaries are detected. In the conventional level-set formulation, the level-set function (LSF) typically develops irregularities during its evolution and needs reinitialization to periodically replace the degraded LSF. Here, we used a variational LSF in which the regularity of the LSF is maintained intrinsically.

After this introduction, the related works will be discussed in Section II. The details of the proposed method will be discussed in Section III. Experimental results will be discussed in Section IV. The results are evaluated in Section V. Section VI highlights the conclusions of this paper.

II. RELATED WORK

Research on subsurface imaging (including seismic methods) is too vast to review here; see [5] for an extensive review. Several semiautomated and automated methods have been introduced in the literature for layer finding and ice thickness in radar images [6]–[20]. Freeman *et al.* [9] finds near-surface ice layers in images from the shallow subsurface radar on NASA’s Mars reconnaissance Orbiter (SHARAD). First, the layers were transformed to horizontal layers and then several filtering and thresholding techniques were applied to enhance the image and discard unclear layers. Finally the layers were transformed back to image space. Our algorithm is quite distinct from this method in the sense that it does not need any intermediate thresholding, which might be different from one image to another. Ferro and Bruzzone [8] proposed an algorithm to extract the deepest scattering area visible in radargrams from the SHARAD mission acquired on the north polar layered deposits of Mars. Their algorithm is based on discriminating the statistical properties of subsurface targets and finding a suitable fitting model. This method is unable to find exact layers in the ice and only provides approximate locations of different subregions based only on the statistical analysis of the signal.

Several works in the literature use graphical models to detect ice layers [6], [14] in radar echograms. Crandall *et al.* [6] used probabilistic graphical models for detecting the ice layer

boundary in echogram images. Their model incorporates several types of evidence and constraints, including that layer boundaries should lie along areas of high image contrast and that layer boundaries should be continuous and not intersect. The extension of this paper was presented in [14] where they used Markov–Chain Monte Carlo to sample from the joint distribution over all possible layers conditioned on an image. A Gibbs sampling instead of dynamic programming-based solver was used for performing inference. The problem with using graphical models is that it needs a lot of training samples (around half of the actual data set), which are ground-truth images labeled manually by a human. Given the fact that manual ice layer detection is a very time-consuming and expensive task, the last three methods are not practical for large data sets.

In another work, Gifford *et al.* [11] compared the performance of two methods, edge-based and active contour, for automating the task of estimating polar ice and bedrock layers from airborne radar data acquired over Greenland and Antarctica. They showed that their edge-based approach offers faster processing, but suffers from lack of continuity and smoothness that active contour provides. In their active contour approach, the contour’s shape is adaptively modified and evaluated to minimize the cost or energy in the image [21], [22]. The main disadvantage of the active contour model is the incapability of maintaining the topology of the evolving curve. This difficulty does not arise in the level-set model as it embeds the evolving curve into a higher dimensional surface. Mitchell *et al.* [15] used a level-set technique for estimating bedrock and surface layers. However, for each single image, the user needs to reinitialize the curve manually and as a result, the method is quite slow and was applied only to a small data set. In this paper, the regularity of level set is intrinsically maintained using a distance regularization term. Therefore, it does not need any manual reinitialization and was automatically applied on a large data set.

III. METHODOLOGY

Here, we propose to use level-set technique to precisely detect the ice surface and the bottom boundary. The level-set method (LSM) is essentially a successor to the active contour method (ACM). The ACM, also known as the Snake Model,

was first introduced by Kass *et al.* [22]. The ACM is designed to detect interfaces and boundaries by a set of parametrized curves (contours) that march successively toward the desired object until the desired interfaces are captured. Assume that these parametrized curves are expressed as

$$C(s, t) = (x(s, t), y(s, t)) \quad s \in [0, 1], \quad t \in [0, \infty) \quad (1)$$

where s is the parameter of the curve length and t is the temporal variable. One can think of the curve $C(s, t)$ as the moving front of a current that approaches the boundaries of the desired object as time increases until it captures the desired interface. The moving current represents a vector field, which in turn influences the motion of the front curve. In our case, this vector field is precisely created based on the properties of the desired feature in the image, so that it can eventually lead the front curve to the boundaries of the desired object.

Therefore, the front curve $C(s, t)$ moves and should eventually capture the interface of the desired object according to the following differential equation:

$$\frac{\partial C}{\partial t} = FN \quad (2)$$

where F is the velocity function for the moving curve C , and N determines the direction of the motion. Here, N is the normal vector to the curve C . Even though the ACM is an efficient tool in image and video segmentation, it suffers from certain serious issues. Being a parametrized approach, the ACM approach can fail, because it is incapable of consistently handling the topology of the front moving curve. In fact, in each iteration, certain parts of the curve C can split or merge, since leading reference points can distance from or come closer to each other; therefore, the topology of the front curve can undergo substantial changes in each iteration. The accumulation of such changes of topology can introduce unnecessary, or even misleading, complexities to the process, which will cause the frontier curve to fail in tracking the right interface in the image. To overcome the disadvantages that the snakes model presents, the LSM was proposed by Osher and Sethian [23]. Rather than following the interface itself as in the ACM, the LSM takes the original curve and builds it into a surface. In other words, the LSM takes the problem to one degree higher in the spatial dimension and considers the curve $C(s, t)$ as the zero-level of a surface $z = \varphi(x, y, t)$ at any given time t . The function φ is called the LSF. We then track the changes of $C(s, t)$ as the 3-D shape φ evolves at each iteration.

More precisely, assume that the curve $C(s, t)$ is the interface of an open region $\Omega_t \subset \mathcal{R}^2$. We embed the curve $C(s, t)$ in the surface $z = \varphi(x, y, t)$ in a way that $C(s, t)$ will be the zero level set of the LSF, φ , which takes negative values inside Ω_t and positive values outside of it; that is

$$\varphi(x, y, t) = 0 \quad \text{for } x \in \partial\Omega_t \quad (3)$$

$$\varphi(x, y, t) < 0 \quad \text{for } \in \Omega_t$$

$$\varphi(x, y, t) > 0 \quad \text{for } \notin \bar{\Omega}_t. \quad (4)$$

The advantage of the LSM is that it handles changes in the topology organically and does not create any unnecessary

complexity. However, this comes with a higher computational price: instead of a 2-D curve, as in the ACM, we are now moving a 3-D object in each iteration. But as mentioned previously, we should only track the zero level set of the surface φ . Therefore, it makes sense to evolve only a narrow band around the zero-level set to reduce the computational cost. In fact, this method has been proposed by the same authors in their later works. We will also take advantage of this computational shortcut as we proceed.

In the setting of the LSM, the LSF, φ , is the solution of the following dynamical system:

$$\frac{\partial \varphi}{\partial t} = -\frac{\partial \mathcal{F}}{\partial \varphi} \quad (x, y, t) \in \Omega \times [0, \infty] \quad (5)$$

with a typical initial condition. In (5), \mathcal{F} represents the level-set functional; conventionally, in image segmentation approaches, the functional \mathcal{F} is defined as the ensemble of several forces, such as the edge and the area forces

$$\mathcal{F} = \mathcal{E}_{\text{edge}} + \mathcal{E}_{\text{area}} \quad (6)$$

where

$$\mathcal{E}_{\text{edge}}(\varphi) = \lambda \int_{\Omega} g \delta(\varphi) |\nabla \varphi| dx \quad (7)$$

$$\mathcal{E}_{\text{area}}(\varphi) = \alpha \int_{\Omega} g H(-\varphi) dx \quad (8)$$

with α and λ being real constants and $\lambda > 0$. The functions δ and H are the Dirac and Heaviside functions, respectively. The function g is the edge indicator on Ω , the area of the image, which is defined by

$$g = \frac{1}{1 + |\nabla G_{\sigma} * I|^2} \quad (9)$$

where I is the image intensity and G_{σ} is a Gaussian kernel with a standard deviation σ .

The edge term $\mathcal{E}_{\text{edge}}$ computes the line integral along the zero-level contour of φ ; that is, $\int_0^1 g(C(s)) |C'(s)| ds$, where the curve $C = C(s) : [0, 1] \rightarrow \Omega$ is the zero-level contour and s is the curve length. This term will be minimized when C is positioned on the boundary of the desired object. The area term, $\mathcal{E}_{\text{area}}$, is basically calculated as a weighted area of the region inside the zero-level contour. It accelerates the motion of the zero-level contours toward the desired object.

Therefore, to minimize the energy functional, \mathcal{F} , it is necessary to solve the following partial differential equation (PDE) system:

$$\begin{aligned} \frac{\partial \varphi}{\partial t} &= \lambda \delta(\varphi) \operatorname{div} \left(g \frac{\nabla \varphi}{|\nabla \varphi|} \right) + \alpha g \delta(\varphi) \\ \varphi(x, 0) &= \varphi_0(x); \quad (x, t) \in \Omega \times [0, \infty). \end{aligned} \quad (10)$$

This system is subject to the no-flux boundary conditions on Ω , which signifies that there is no external force outside the image area. To carry out a numerical process to solve this PDE system, the spatial derivatives are discretized using the upwind scheme. The use of the central difference scheme will result in instability in the numerical procedure. The numerical procedure also involves the assumption that $|\nabla \varphi| = 1$. We initialize the procedure with a function that satisfies this property, but the numerical scheme will not pass on this

property; consequently, at each step, an extra care, known as reinitialization, must be taken to avoid the error accumulation. The reinitialization procedure involves solving the following PDE system for ψ in each step:

$$\frac{\partial \psi}{\partial t} = \text{sign}(\varphi)(1 - |\nabla \psi|). \quad (11)$$

This severely slows down the computation. To overcome this difficulty, we use the distance-regularized level-set evolution (DRLSE) method as proposed in [24]—also see [21]. In the DRLSE method, the level-set functional \mathcal{F} is defined as

$$\mathcal{F} = \mathcal{E}_{\text{edge}} + \mathcal{E}_{\text{area}} + \mathcal{E}_p \quad (12)$$

where \mathcal{E}_p represents the distance regularization term defined by

$$\mathcal{E}_p(\varphi) = \mu \int_{\Omega} p |\nabla \varphi| dx \quad (13)$$

with a potential function p and a constant $\mu > 0$. As suggested in [24], we use a double-well function for the potential function p as follows:

$$p(s) = \begin{cases} (1 - \cos(2\pi s))/4\pi^2, & s \leq 1 \\ (s - 1)^2/2, & s \geq 1 \end{cases} \quad (14)$$

with $s \in [0, \infty)$.

We have

$$\frac{\partial \mathcal{E}_p}{\partial \varphi} = -\mu \text{div}(D \nabla \varphi) \quad (15)$$

where the diffusion coefficient $D = D(\varphi)$ is given by

$$D(\varphi) = \frac{p'(|\nabla \varphi|)}{|\nabla \varphi|}. \quad (16)$$

It is discussed in [24] that p has two minimum points at $s = 0$ and $s = 1$; and it is twice differentiable with the following properties:

$$\left| \frac{p'(s)}{s} \right| < 1 \quad \text{for } s > 0$$

and

$$\lim_{s \rightarrow 0} \frac{p'(s)}{s} = \lim_{s \rightarrow \infty} \frac{p'(s)}{s} = 1. \quad (17)$$

Given the above-mentioned properties, one can easily see that

$$\left| \mu \frac{p'(|\nabla \varphi|)}{|\nabla \varphi|} \right| \leq \mu. \quad (18)$$

That means the diffusion coefficient in (15) remains bounded. Now, the new energy functional \mathcal{F} can be minimized by solving the following gradient flow:

$$\begin{aligned} \frac{\partial \varphi}{\partial t} &= \lambda \delta(\varphi) \text{div} \left(g \frac{\nabla \varphi}{|\nabla \varphi|} \right) + \alpha g \delta(\varphi) + \mu \text{div}(D \nabla \varphi) \\ \varphi(x, 0) &= \varphi_0(x) \\ (x, t) &\in \Omega \times [0, \infty). \end{aligned} \quad (19)$$

Thanks to the distance regularization term, the central difference scheme can be used to discretize spatial derivatives, which leads to a stable numerical procedure without the need of reinitialization.

It must also be noted that, in practice, the functions δ and H are approximated by the smooth functions δ_ε and H_ε defined by

$$\delta_\varepsilon(x) = \begin{cases} \frac{1}{2\varepsilon} \left(1 + \cos \left(\frac{\pi x}{\varepsilon} \right) \right), & |x| \leq \varepsilon \\ 0, & |x| > \varepsilon \end{cases} \quad (20)$$

$$H_\varepsilon(x) = \begin{cases} \frac{1}{2} \left(1 + \frac{x}{\varepsilon} + \frac{1}{\pi} \sin \left(\frac{\pi x}{\varepsilon} \right) \right), & |x| \leq \varepsilon \\ 1, & |x| > \varepsilon \\ 0, & |x| < -\varepsilon \end{cases} \quad (21)$$

for $\varepsilon > 0$. ε is often considered to be $3/2$.

As mentioned before, the above-mentioned equation is governed by the no-flux boundary condition. For the initial condition, we will consider a simple step function defined by

$$\varphi_0 = \begin{cases} -c_0, & x \in \Omega_0 \\ c_0, & x \in \Omega/\Omega_0 \end{cases} \quad (22)$$

where $c_0 > 0$ is a constant, and Ω_0 is a region inside the image region Ω .

IV. EXPERIMENTAL RESULTS

We tested our ice layer identification approach on publicly available radar images from the 2009 NASA Operation IceBridge Mission. The images were collected with the airborne Multichannel Coherent Radar Depth Sounder system described in [2]. The images have a resolution of 900 pixels in the horizontal direction, which covers around 50 km on the ground, and 700 pixels in the vertical direction, which corresponds to 0–4 km of ice thickness. For these images, there are manually picked interfaces and we compare our ice layer identification approach with them. The manually picked interfaces have been produced by human annotators and some of them are inaccurate and contain only one layer. We chose the images that have both ice surface and bottom layers and tested our method on a total of 323 images. Fig. 2 shows the corresponding map and data segments of our entire data set from CREsis website (<https://data.cresis.ku.edu/data/rds/>). Since our method is fully automatic, we do not need any training data set and our method is not affected by inaccurate ground truth. Moreover, human annotation is quite time-consuming and because our method does not need any training and is independent of ground-truthing, it is quite fast. We used the same iteration number of 800 for all of the images.

Fig. 3–6 show the results of our approach with respect to the manually picked interfaces in a diverse data set, which includes images with clutter from englacial scattering, large variability of the subglacial topography, surface multiples, and faint ice bottoms.

A. Clutter

It was explained in the introduction that there are several challenges in automatic processing of radar imagery. The first challenge is low SINR. All of the images in our data set contain clutter from englacial scattering. For example, Fig. 3–6 show the representative images that contain clutter. The background noise did not affect the performance of our

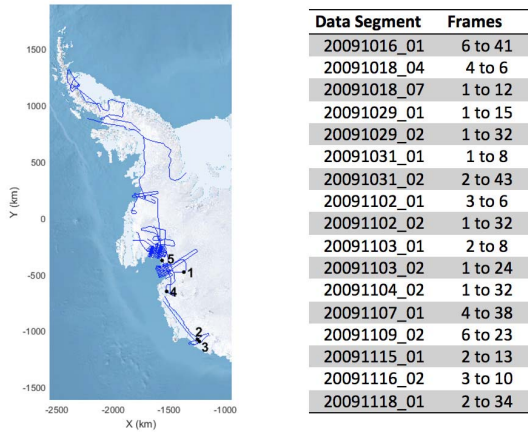


Fig. 2. Map and data segments used in this paper. Blue lines show all analyzed flight lines. Black dots numbered 1–5 are for 1—Fig. 1 (left) (frame ID 20091102_02_008), 2—Fig. 3 (frame ID 20091016_01_021), 3—Figs. 1 (right) and 4 (frame ID 20091016_01_026), 4—Fig. 5 (frame ID 20091102_02_023), and 5—Fig. 6 (frame ID 20091102_02_032).

proposed technique. Fig. 3(a) shows the initial curve. This initial curve was drawn automatically and there is no need for user input in any step of the procedure. Fig. 3(b)–(e) shows the results after iteration 200, 400, 600, and 800, respectively. As it can be seen in Fig. 3(b), after 200 iterations, the ice surface is approximately detected, but the ice bottom is still not detected. After 400 iterations, part of the ice bottom is detected, but after 800 iterations, both the ice surface and bottom layers are detected perfectly. Fig. 3(f) shows the manually picked interfaces, which is the result of labeling the layers by a human operator. Comparing Fig. 3(e), the result of the proposed approach, with Fig. 3(f), the manually picked interfaces, we notice that our result is very close to the manually picked interfaces and appears to be even more accurate in some parts as shown in Fig. 3(g) and (h). The automated approach removes much of the tedium from the task by providing automated results for most of the ice bottom and allowing the operator to focus on the harder to track regions where the automated algorithm fails.

B. Diverse Subglacial Topology

The subglacial topography can vary from a smooth shape to a very rough topology due to variation in landscape relief. Fig. 4 shows an example where the ice bottom is rougher. The same initial curve as the previous example was utilized in Fig. 4(a). After 400 iterations [Fig. 4(c)], the approximate shape of the ice surface and bottom is detected. After 600 iterations, the solution is converged and the exact shape of both layers is detected. Here, we continued the iteration to 800 to have the same conditions for all images. As can be seen in Fig. 4(d), the perfect shapes of the ice surface and bottom are maintained, and the extra iterations did not make the situation worse. Comparing our results [Fig. 4(d)] with the manually picked interfaces [Fig. 4(e)], we find that our results are more smooth and accurate than the manually picked interfaces. Fig. 4(f) and (g) shows the magnified sections of images in Fig. 4(d) and (e).

C. Surface Multiple

Strong surface reflections can occur due to reflecting the energy back from the ice sheet surface to the receiver antenna and back to the surface again. The surface multiple is another challenging factor in processing and identification of the ice surface and bottom. Fig. 5 shows an example of a surface multiple with a more complicated shape of ice bottom and with a high level of clutter in the image. Here, it takes the full 800 iterations for the level-set solution to converge, but it shows a satisfactory results compared with the manually picked interfaces. This representative result shows the robustness of our algorithm to the surface multiple.

V. EVALUATION

To evaluate the performance of our approach, first we need to set up some benchmarks. For any particular pixel in the image that we are evaluating, there are four cases in comparison with the manually picked interfaces (ground truth); these four cases are true positive (TP) or correct result, false positive (FP) or unexpected result, false negative (FN) or missing results, and finally true negative (TN) [25]. For example, in a radar image, pixels that are located on the interfaces in the ground-truth image and are classified the same by our method are TP. Pixels that are not on any interfaces in the ground-truth image and are not classified in any of them by our method are TN, and so on. From the confusion matrix, precision (P) and recall (R) are calculated as follows:

$$R = \frac{TP}{TP + FN} \quad (23)$$

$$P = \frac{TP}{TP + FP} \quad (24)$$

Precision, the exactness of a classifier, and recall, the completeness of a classifier, can be combined to produce a single metric known as *F-measure*, which is the weighted harmonic mean of precision and recall. The F-measure defined as

$$F = \frac{1}{\alpha \frac{1}{p} + (1 - \alpha) \frac{1}{r}} = \frac{(\beta^2 + 1)PR}{\beta^2 P + R} \quad (25)$$

captures the precision and recall tradeoff. The F-measure is valued between 0 and 1, where larger values are more desirable. In this paper, we used a balanced F-measure, i.e., with $\beta = 1$.

The assumption is that human labeled images (ground truth) contain perfect results and then the performance of our method was evaluated with respect to manually picked interfaces. We calculated the precision, recall, and F-measure for all of the images in the data set. Around 65% of the images in our data set have invisible or faint ice bottom due to attenuation of radio-waves by thick warm ice. For the images that ice bottom is not completely visible in the image (Fig. 6), our approach is not able to detect the invisible part accurately. For these images, it is better to stop the iteration early, otherwise its error will be accumulated. However, to avoid human interference, we kept the 800th iteration for all of the images and reached 75% F-measure for the entire data set. For the images that have visible ice bottom layers (1/3 of data set), we reached the average F-measure of 96% (Table I).

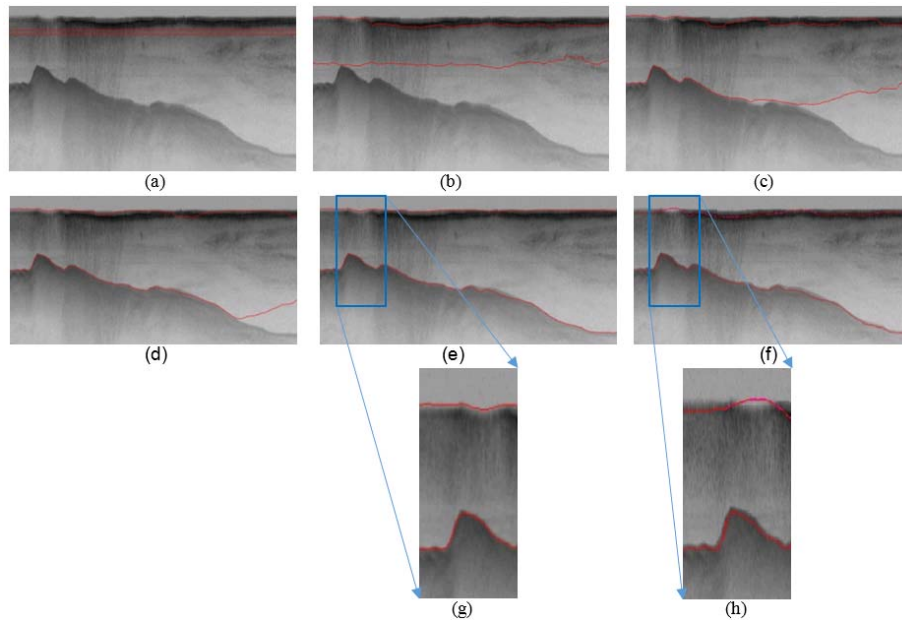


Fig. 3. Contour evolution throughout processing. (a) Initial curve. (b)–(e) Contour adaptation to ice surface and bottom layers after 200, 400, 600, and 800 iterations correspondingly. (f) Manually picked interfaces. (g) and (h) Magnified section of (e) and (f).

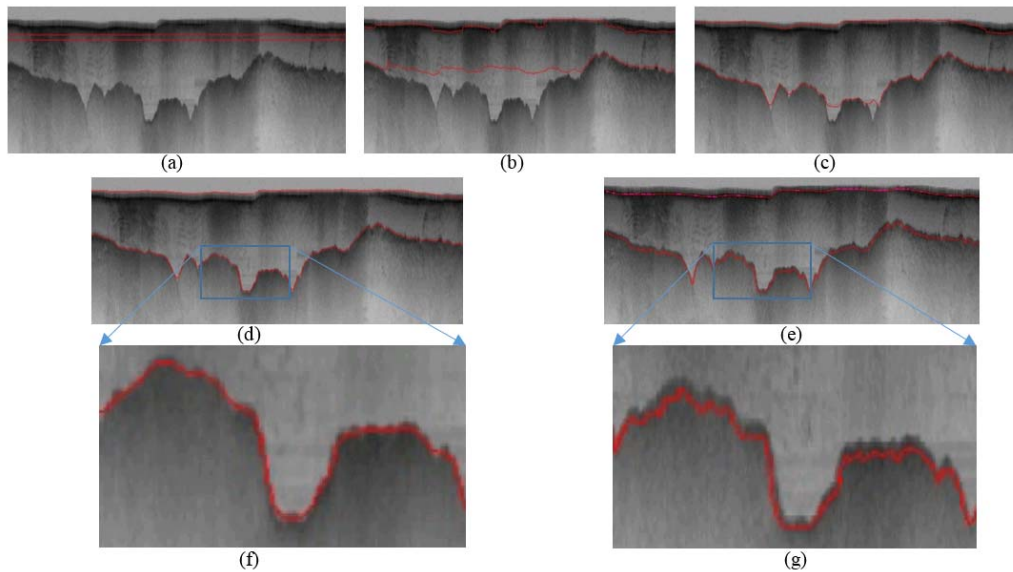


Fig. 4. Contour evolution throughout processing. (a) Initial curve. (b)–(d) Contour adaptation to ice surface and bottom after 200, 400, and 800 iterations correspondingly. (e) Manually picked interfaces. (f) and (g) Magnified section of (d) and (e).

TABLE I
AVERAGE F-MEASURE OF OUR APPROACH FOR THE ENTIRE DATA SET AND ALSO FOR THE IMAGES WITH VISIBLE ICE BOTTOM

	F-measure
Entire dataset (visible and invisible ice bottom)	75%
Images with visible ice bottom	96%

TABLE II
MEAN AND MEDIAN ERROR ON ICE SURFACE AND BOTTOM

Metrics	Ice Surface	Ice Bottom
Mean Error (pixel)	11.15	6.60
Median Error (pixel)	6.56	2.07

We also calculated the accuracy by computing the mean absolute deviation between the manually picked and the estimated layer boundaries by our algorithm. We used two summary statistics: mean columnwise absolute error over all images in the visible dataset and the median of the columnwise mean absolute errors across images (Table II).

Our algorithm is very fast, taking an average of 30 s to process each image on a 2.7-GHz machine. Moreover, it does not need any training phase with human-labeled images, which speeds up the entire process significantly. Usually, it takes up to 5–10 min per file to manually label the image [11].

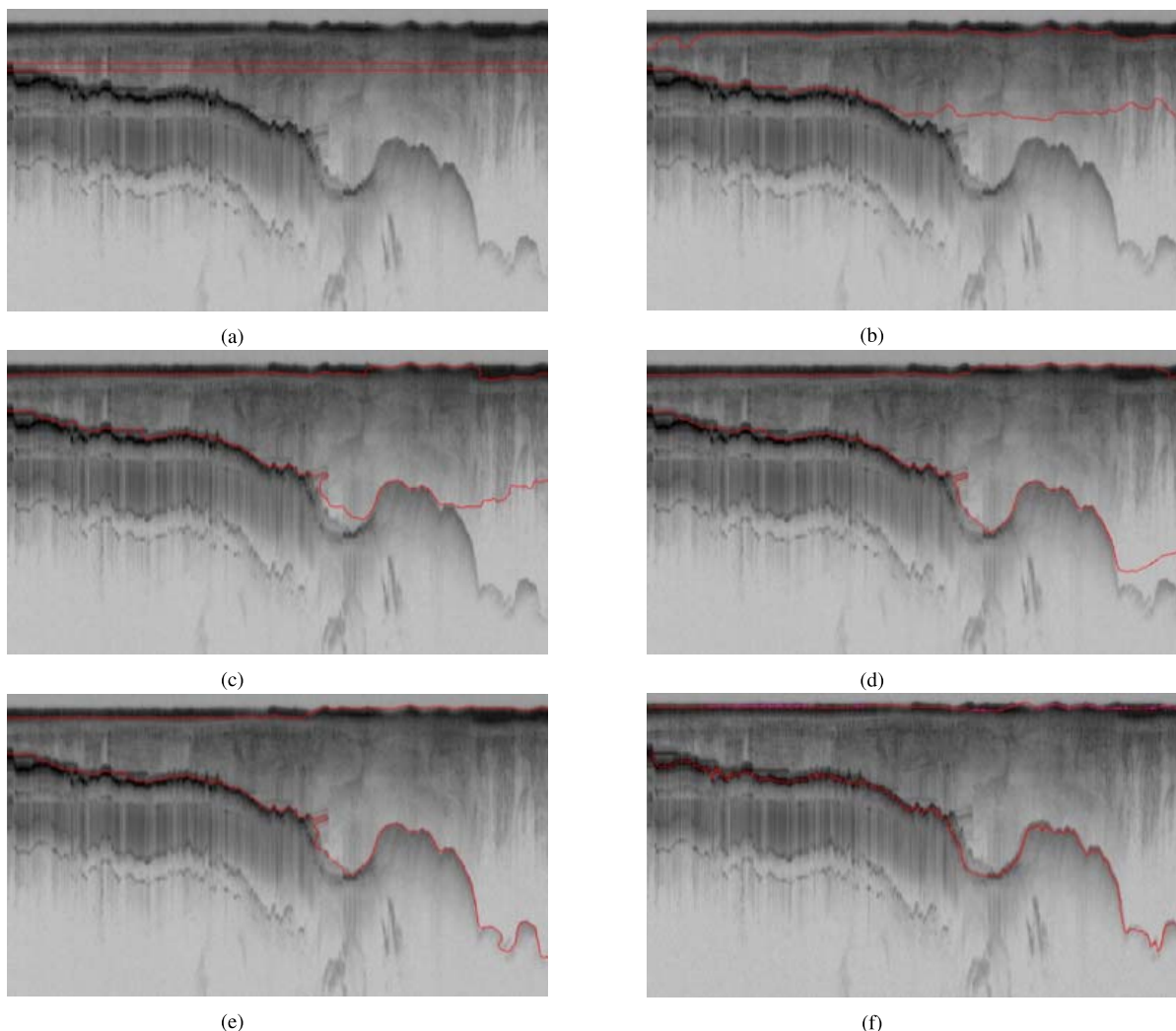


Fig. 5. Contour evolution throughout processing. (a) Initial curve. (b)–(e) Contour adaptation to ice surface and bottom after 200, 400, 600, and 800 iterations, respectively. (f) Manually picked interfaces.

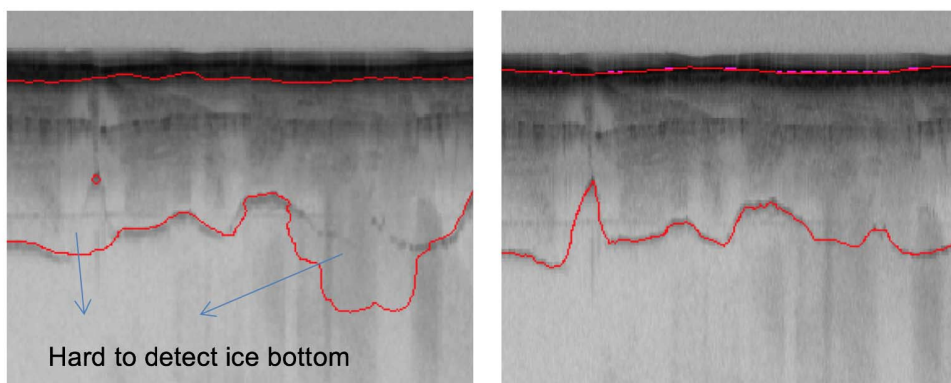


Fig. 6. Our approach is not able to detect the invisible parts of ice bottom. Left: ice surface and bottom detected by our approach. Right: manually picked interfaces.

VI. CONCLUSION AND FUTURE WORK

We presented an automatic approach to estimate ice surface and bottom in radar echo sounding imagery. In this approach, the complex topology of ice surface and bottom was detected by evolving an initial curve using distance-regularized level set. The results were evaluated on a large data set of airborne radar imagery collected during the IceBridge Mission over

Antarctica and show promising results with respect to hand-labeled ground truth. We reached the high accuracy of 75% for the entire data set, which contains images with noise, diverse ice bottom topology, surface multiples, and faint ice bottom echoes using a fully automatic technique. Our algorithm is robust to noise and surface multiples and can detect subglacial topography with a smooth or rough shape. For images without

the faint subglacial topography, we reached the F-measure of 96%. However, 65% of the images in the data set present faint or invisible ice bottoms. For those images, it is better to first separate them from the images that have a visible ice bottom layer and then apply our algorithm with a different numbers of iterations. In the future, we are planning to extend this paper by improving the quality of the images with faint or currently undetectable ice bottom signals prior to applying the level-set algorithm. In the future, we will look at other data sets especially those with internal ice layers. We will also try to implement the Viterbi method [19], [20] for providing a faster solution in comparison with the level-set algorithm.

REFERENCES

- [1] A. Shepherd *et al.*, "A reconciled estimate of ice-sheet mass balance," *Science*, vol. 338, no. 6114, pp. 1183–1189, 2012.
- [2] C. Allen *et al.*, "Antarctic ice depth sounding radar instrumentation for the NASA DC-8," *IEEE Aerosp. Electron. Syst. Mag.*, vol. 27, no. 3, pp. 4–20, Mar. 2012.
- [3] C. Leuschen, *IceBridge Snow Radar LIB Geolocated Radar Echo Strength Profiles*. NASA DAAC at the National Snow and Ice Data Center, Boulder, CO, USA, 2014, doi:10.5067/05LF3JANL511.
- [4] S. Gogineni *et al.*, "Bed topography of jakobshavn isbrae, greenland, and byrd glacier, antarctica," *J. Glaciol.*, vol. 60, no. 223, pp. 813–833, 2014.
- [5] A. S. Turk, K. A. Hocaoglu, and A. A. Vertiy, *Subsurface Sensing*, vol. 197. Hoboken, NJ, USA: Wiley, 2011.
- [6] D. J. Crandall, G. C. Fox, and J. D. Paden, "Layer-finding in radar echograms using probabilistic graphical models," in *Proc. 21st Int. Conf. Pattern Recognit. (ICPR)*, Nov. 2012, pp. 1530–1533.
- [7] M. Fahnestock, W. Abdalati, S. Luo, and S. Gogineni, "Internal layer tracing and age-depth-accumulation relationships for the northern Greenland ice sheet," *J. Geophys. Res.*, vol. 106, no. D24, pp. 33789–33797, 2001.
- [8] A. Ferro and L. Bruzzone, "A novel approach to the automatic detection of subsurface features in planetary radar sounder signals," in *Proc. IEEE Int. Geosci. Remote Sens. Symp. (IGARSS)*, Jul. 2011, pp. 1071–1074.
- [9] G. J. Freeman, A. C. Bovik, and J. W. Holt, "Automated detection of near surface Martian ice layers in orbital radar data," in *Proc. IEEE Southwest Symp. Image Anal. Interpretation (SSIAI)*, May 2010, pp. 117–120.
- [10] H. Frigui, K. C. Ho, and P. Gader, "Real-time landmine detection with ground-penetrating radar using discriminative and adaptive hidden Markov models," *EURASIP J. Adv. Signal Process.*, vol. 2005, no. 12, pp. 1867–1885, 2005.
- [11] C. M. Gifford, G. Finyom, M. Jefferson, Jr., M. Reid, E. L. Akers, and A. Agah, "Automated polar ice thickness estimation from radar imagery," *IEEE Trans. Image Process.*, vol. 19, no. 9, pp. 2456–2469, Sep. 2010.
- [12] A.-M. Ilisei, A. Ferro, and L. Bruzzone, "A technique for the automatic estimation of ice thickness and bedrock properties from radar sounder data acquired at Antarctica," in *Proc. IEEE Int. Geosci. Remote Sens. Symp. (IGARSS)*, Jul. 2012, pp. 4457–4460.
- [13] N. B. Karlsson, D. Dahl-Jensen, S. P. Gogineni, and J. D. Paden, "Tracing the depth of the Holocene ice in North Greenland from radio-echo sounding data," *Ann. Glaciol.*, vol. 54, no. 64, pp. 44–50, 2013.
- [14] S. Lee, J. Mitchell, D. J. Crandall, G. Fox, and G. C. Fox, "Estimating bedrock and surface layer boundaries and confidence intervals in ice sheet radar imagery using MCMC," in *Proc. IEEE Int. Conf. Image Process. (ICIP)*, Oct. 2014, pp. 111–115.
- [15] J. E. Mitchell, D. J. Crandall, G. C. Fox, M. Rahnemoonfar, and J. D. Paden, "A semi-automatic approach for estimating bedrock and surface layers from multichannel coherent radar depth sounder imagery," *Proc. SPIE*, vol. 8892, pp. 88921E–88926E, Oct. 2013.
- [16] J. E. Mitchell, D. J. Crandall, G. Fox, and J. D. Paden, "A semi-automatic approach for estimating near surface internal layers from snow radar imagery," in *Proc. IGARSS*, Jul. 2013, pp. 4110–4113.
- [17] L. C. Sime, R. C. A. Hindmarsh, and H. Corr, "Instruments and Methods Automated processing to derive dip angles of englacial radar reflectors in ice sheets," *J. Glaciol.*, vol. 57, no. 202, pp. 260–266, 2011.
- [18] C. Panton, "Automated mapping of local layer slope and tracing of internal layers in radio echograms," *Ann. Glaciol.*, vol. 55, no. 67, pp. 71–77, 2014.
- [19] B. Smock and J. Wilson, "Reciprocal pointer chains for identifying layer boundaries in ground-penetrating radar data," in *Proc. IEEE Int. Geosci. Remote Sens. Symp. (IGARSS)*, Jul. 2012, pp. 602–605.
- [20] B. Smock and J. Wilson, "Efficient multiple layer boundary detection in ground-penetrating radar data using an extended Viterbi algorithm," *Proc. SPIE*, vol. 8357, p. 83571X, May 2012.
- [21] T. F. Chan and L. A. Vese, "Active contours without edges," *IEEE Trans. Image Process.*, vol. 10, no. 2, pp. 266–277, Feb. 2001.
- [22] M. Kass, A. Witkin, and D. Terzopoulos, "Snakes: Active contour models," *Int. J. Comput. Vis.*, vol. 1, no. 4, pp. 321–331, 1988.
- [23] S. Osher, "Fronts propagating with curvature-dependent speed: Algorithms based on Hamilton-Jacobi formulations," *J. Comput. Phys.*, vol. 79, no. 1, pp. 12–49, 1988.
- [24] X. Chen, C. Wang, and H. Zhang, "DEM generation combining SAR polarimetry and shape-from-shading techniques," *IEEE Geosci. Remote Sens. Lett.*, vol. 6, no. 1, pp. 28–32, Jan. 2009.
- [25] D. M. Powers, "Evaluation: From precision, recall and F-measure to ROC, informedness, markedness and correlation," *J. Mach. Learn. Technol.*, vol. 2, no. 1, pp. 37–63, 2011.



Maryam Rahnemoonfar (S'08–M'12) received the M.Sc. degree in remote sensing from the University of Tehran, Tehran, Iran, in 2005, and the Ph.D. degree in computer science from the University of Salford, Manchester, U.K., in 2010.

She is currently an Assistant Professor of Computer Science and the Director of the Computer Vision and Remote Sensing Laboratory (Bina Laboratory), Texas A&M University at Corpus Christi, Corpus Christi, TX, USA. Her research interests include image processing, computer vision, machine learning, remote sensing, and synthetic aperture radar.



Geoffrey Charles Fox received the Ph.D. degree in theoretical physics from Cambridge University, Cambridge, U.K.

He is currently a Distinguished Professor of Computing, Engineering, and Physics with Indiana University Bloomington, Bloomington, IN, USA, where he is also the Director of the Digital Science Center and the Chair of the Intelligent Systems Engineering Department, School of Informatics and Computing. His research interests include applying computer science from infrastructure to analytics in biology, pathology, sensor clouds, earthquake and ice-sheet science, image processing, deep learning, network science, financial systems, and particle physics. The infrastructure work is built around software-defined systems on clouds and clusters. The analytics focuses on scalable parallelism.

Dr. Fox is a Fellow of American Physical Society and the Association for Computing Machinery.



Masoud Yari received the Ph.D. degree in applied mathematics from Indiana University Bloomington, Bloomington, IN, USA, in 2008.

He is currently an Assistant Professor of Computer Science and Applied Mathematics with Texas A&M University at Corpus Christi, Corpus Christi, TX, USA. His research interests include scientific computing, machine learning, mathematical biology, partial differential equations, dynamical systems, image processing, and pattern recognition.



John Paden (S'95–M'06) received the M.S. and Ph.D. degrees in electrical engineering from The University of Kansas (KU), Lawrence, KS, USA, with a focus on radar signal and data processing for the remote sensing of the cryosphere.

He joined Vexcel Corporation, Boulder, CO, USA, which is a remote sensing company, where he was a Systems Engineer and an SAR Engineer for three and a half years. He joined the Center for Remote Sensing of Ice Sheets, KU, in 2010, where he led the signal and data processing efforts and is currently a

Research Faculty Member.